



HAL
open science

Observational 2D model of H₂ emission from a bow shock in the Orion Molecular Cloud

Lars E. Kristensen, T. L. Ravkilde, Guillaume Pineau-Des-Forêts, Sylvie Cabrit, D. Field, Maiken Gustafsson, Stephan Diana, Jean-Louis Lemaire

► **To cite this version:**

Lars E. Kristensen, T. L. Ravkilde, Guillaume Pineau-Des-Forêts, Sylvie Cabrit, D. Field, et al.. Observational 2D model of H₂ emission from a bow shock in the Orion Molecular Cloud. *Astronomy and Astrophysics - A&A*, 2008, 477, pp.203-211. 10.1051/0004-6361:20078100 . hal-03785610

HAL Id: hal-03785610

<https://hal.science/hal-03785610>

Submitted on 6 Oct 2022

HAL is a multi-disciplinary open access archive for the deposit and dissemination of scientific research documents, whether they are published or not. The documents may come from teaching and research institutions in France or abroad, or from public or private research centers.

L'archive ouverte pluridisciplinaire **HAL**, est destinée au dépôt et à la diffusion de documents scientifiques de niveau recherche, publiés ou non, émanant des établissements d'enseignement et de recherche français ou étrangers, des laboratoires publics ou privés.

Observational 2D model of H₂ emission from a bow shock in the Orion Molecular Cloud^{*}

L. E. Kristensen¹, T. L. Ravkilde², G. Pineau des Forêts^{1,3}, S. Cabrit¹, D. Field², M. Gustafsson⁴, S. Diana¹, and J.-L. Lemaire¹

¹ Observatoire de Paris & Université de Cergy-Pontoise, LERMA, UMR 8112 du CNRS, 92195 Meudon Cedex, France
e-mail: lars.kristensen@u-cergy.fr

² Department of Physics and Astronomy, University of Aarhus, 8000 Aarhus C, Denmark

³ Institut d'Astrophysique Spatiale, UMR 8617 du CNRS, Université de Paris Sud, 91405 Orsay, France

⁴ Max Planck Institut für Astronomie, 69117 Heidelberg, Germany

Received 15 June 2007 / Accepted 24 October 2007

ABSTRACT

Aims. We present a new method for reproducing high spatial resolution observations of bow shocks by using 1D plane parallel shock models. As an example we analyse one bow shock located in the Orion Molecular Cloud (OMC1).

Methods. We use high spatial resolution near-infrared observations of H₂ rovibrational emission to constrain shock models. These observations have been made at the ESO-VLT using a combination of the NACO adaptive optics system and infrared camera array and the Fabry-Perot interferometer. Three rovibrational H₂ lines have been observed: $v = 1-0$ S(1) at 2.12 μm , $v = 1-0$ S(0) at 2.23 μm and $v = 2-1$ S(1) at 2.25 μm . The spatial resolution is $0''.15 \sim 70$ AU. We analyse a single bow shock located in our field, featuring a very well defined morphology and high brightness.

Results. One dimensional shock models are combined to estimate the physical properties of pre-shock density, shock velocity and transverse magnetic field strength along the bow shock. We find that the pre-shock density is constant at $\sim 5 \times 10^5 \text{ cm}^{-3}$ and shock velocities lie between $\sim 35 \text{ km s}^{-1}$ in the wings of the shock and $\sim 50 \text{ km s}^{-1}$ at the apex. We also find that the transverse magnetic field is stronger at the apex and weaker further down the wings varying between ~ 2 and 4 mGauss. Predictions of shock velocity and magnetic field strength agree with previous independent observations.

Key words. ISM: individual objects: OMC1 – ISM: kinematics and dynamics – ISM: molecules – shock waves – ISM: lines and bands

1. Introduction

With this work we present a new method for analysing bow shocks caused by outflows. These shocks may originate from a multitude of objects ranging from young stellar objects (YSOs), planetary nebulae, supernova explosions, neutron stars to active galactic nuclei. In this paper we will limit our focus to jets and outflows from YSOs.

Although jets and outflows from YSOs were not predicted as a natural consequence of any unified theoretical model of star formation, observations show that they are an integral part of star formation. Jets and outflows play an important role both in the formation of individual stars, but also in inducing new generations of stars (e.g. Elmegreen & Lada 1977; Vannier et al. 2001). Therefore by observing and modelling shocks it is possible to gain significant insight into the physical conditions found in star forming regions (see e.g. Smith et al. 2003; Giannini et al. 2006; Neufeld et al. 2006; Kristensen et al. 2007, for recent results) providing new constraints for models of clustered star formation.

The Orion Molecular Cloud (OMC1) is the closest site of active massive star formation located at a distance of ~ 460 pc (Bally et al. 2000). Here more than 1000 stars have formed around the Trapezium OB association within the last 1 Myr (Hillenbrand et al. 1998). On the surface of OMC1 an outflow was launched approximately centred on the Becklin-Neugebauer

object (BN, a B3 star; Gezari et al. 1998). This resulted in the launch of more than 50 so-called “fingers”. At the apex of each finger a fast moving “bullet” is found (Axon & Taylor 1984; Lee & Burton 2000; Doi et al. 2002), a dissociative shock which is observed in [FeII] emission with H₂ emission trailing behind in prominent bow shocks (Allen & Burton 1993). The fingers are mostly found to the northwest of BN and shock velocities are measured from proper motions to be several hundred km s^{-1} (Lee & Burton 2000; Doi et al. 2002). This gives a dynamical age of the outflow of ~ 1000 years.

The same event or a similar event launched a series of slower non-dissociative shocks, primarily located southwest of BN ($v \leq 50 \text{ km s}^{-1}$; Chrysostomou et al. 1997; Gustafsson et al. 2003; Cunningham 2006; Nissen et al. 2007). Although the launch mechanism remains a mystery, there is growing consensus that the joint interaction of radio source I, radio source n and possibly BN play a central role (Menten & Reid 1995; Gezari et al. 1998; Beuther et al. 2004; Bally & Zinnecker 2005; Nissen et al. 2007) as these objects were all located within a radius of $2''$ (~ 900 AU) some 500 years ago (Gómez et al. 2005).

Using high spatial resolution observations (i.e. a spatial resolution better than $\sim 0''.5$ or ~ 230 AU) it is possible to resolve individual outflow objects and describe their morphology (e.g. Smith et al. 1997; Stolovy et al. 1998; Schultz et al. 1999; Vannier et al. 2001; Gustafsson et al. 2003; Lacombe et al. 2004; Nissen et al. 2007; Kristensen et al. 2007). In most objects in the slower outflow SW of BN the morphology is clearly bow shaped leading

^{*} Based on observations obtained at the European Southern Observatories, VLT, Chile.

to the interpretation that these objects are indeed bow shocks. In this paper we will analyse one of these bow shocks, which has recently been observed with the ESO-VLT. These new data show a spatial resolution of $0''.13$ (~ 60 AU; Gustafsson 2006; Gustafsson et al. 2007).

Several groups have already constructed 3D bow shock models (e.g. Smith & Brand 1990; Raga et al. 2002; Smith et al. 2003) or 2D models (e.g. Raga & Cabrit 1993; Lee et al. 2001; Ostriker et al. 2001; Lim et al. 2002; Fragile et al. 2005), but so far they do not include detailed chemical reaction networks or the full set of magneto-hydrodynamical equations in a self-consistent manner. By contrast these factors are included in 1D models (e.g. Flower & Pineau des Forêts 2003). However in a 1D model geometry is essentially not defined. Here we make a first attempt to combine both a self-consistent treatment of the chemistry and physics with the geometry.

A common method for constructing 2D/3D bow shocks is to align plane parallel 1D shock models along a predefined bow shape. The shape of the bow is then varied as well as the input parameters for each shock model. Continuity of output parameters along the shock is ensured by letting the input parameters change following simple algorithms (e.g. Smith & Brand 1990; Smith et al. 2003).

In this paper we will start with observations and from these create a 2D shock model. This is done by cutting the bow into segments and then reproducing the observed properties of each segment by a 1D model. This resembles the method mentioned above with respect to constructing a bow shock from 1D models. However, it is important to realise that we let nature dictate the bow shape and how velocity, density, magnetic field strength etc. change instead of assuming an algorithm for the changes. We do this in a very simplified manner ignoring any 3D effects such as inclination and depth.

The method outlined in this paper will provide a first estimation of how initial conditions change along the bow. This can be used to verify the assumptions usually made on how the velocity changes along the bow, but it can also serve as an input parameter for 3D models currently under construction (Ravkilde et al. 2007).

In Sect. 2 we describe how observations were made and in Sect. 3 we provide the observational results. Here we show how our 2D model is assembled and in Sect. 4 we analyse the bow shock following this recipe. Concluding remarks are given in Sect. 5.

2. Observations and data reduction

Observations were performed on the nights of December 3–5, 2004 at the ESO-VLT using the NAOS-CONICA adaptive optics system and infrared camera. The Fabry-Perot (FP) interferometer was used to scan three fields centred on the BN object and covering Peak 1 and 2 located northwest and southeast of BN respectively (Beckwith et al. 1978, see Fig. 1). Full data-reduction has been described in Gustafsson (2006) and Gustafsson et al. (2007). Here we will give a brief overview of data-reduction and focus on the parts relevant for this work. In Fig. 1 we show the full field of our observations in the $v = 1-0$ S(0) transition. The object we have chosen to analyse is located in the field south of BN and we will focus on data reduction of this field.

With the FP we scanned the three H₂ rovibrational lines $v = 1-0$ S(1) at $2.12 \mu\text{m}$, $v = 1-0$ S(0) at $2.23 \mu\text{m}$ and $v = 2-1$ S(1) at $2.25 \mu\text{m}$. The bandwidth of the FP is ~ 2 nm giving a spectral resolution of $\Delta\lambda/\lambda = 1000$. Each line was scanned in 15–18 steps and the exposure time of each frame in the scan

was 120 s. We performed one scan of the $v = 1-0$ S(1) line and 4 scans of the $v = 1-0$ S(0) and $v = 2-1$ S(1) lines. We used the S27 camera with a pixel scale of 27 mas and a field-of-view of $27''.6 \times 27''.6$.

For observations of this field we used the star Parenago 1839 ($m_V = 14.6$) as guide star for the AO system. The visible wavefront sensor was used in all observations.

The Ar line at $2.0992 \mu\text{m}$ was scanned before each science scan to obtain an accurate wavelength calibration. Data reduction included dark and bias subtraction, flat-fielding, bad pixel rejection and wavelength correction contained in the phase map (Gustafsson et al. 2003). Phase maps were obtained from images made from data in the wings of the lines. For each pixel we fitted and integrated a lorentzian profile in the wavelength direction to obtain the integrated brightness.

In the case of the $v = 1-0$ S(0) and $v = 2-1$ S(1) emission lines we performed 4 scans of each line. The resulting brightness maps of these scans have been combined into one. This was done after carefully checking image registration (see below).

The spatial resolution is obtained from the full width at half maximum (*FWHM*) of observed Point-Spread-Functions (PSFs) of stars located in the field. Resolution is on average $0''.13$ corresponding to ~ 5 pixels or ~ 60 AU. This average covers a range of resolutions from $0''.10$ – $0''.17$ (45–80 AU). To improve S/N we have smoothed all images by a 3×3 boxcar moving average. This has degraded the resolution by $\sim 18\%$ to $0''.15$ or ~ 70 AU.

Absolute calibration have been performed by observing the DENIS standard star HR1950, spectral type B1.5V, located at $05^{\text{h}}40^{\text{m}}37^{\text{s}}.30$; $-02^{\circ}49'30''.85$ with a *K*-band magnitude of 6.785 ± 0.024 (Skrutskie et al. 2006). Observations and data reduction of the standard star has been performed in the same manner as the science observations. The star TCC0016 located in our field has been used to verify the calibration. It is a *K7* star whose *K'* magnitude is given by McCaughrean & Stauffer (1994) ($m_{K'} = 8.63$). The two calibrations agree within 10%.

For our data analysis we also need to consider the following issues: (i) atmospheric absorption, (ii) differential reddening and (iii) image registration. In the following we will consider each of these.

(i) When comparing brightness of different lines it is essential that these are as free as possible of differential effects. The atmospheric absorption atlas by Livingston & Wallace (1991) shows that there is little or no absorption for the three lines considered here (see also Kristensen et al. 2007).

(ii) Due to interstellar dust the three lines will suffer from differential reddening or extinction. Brand et al. (1988) and Rosenthal et al. (2000) estimated the extinction in Peak 1 to the north of our object to be 1mag at $2.12 \mu\text{m}$. Mathis (1990) showed empirically that the differential reddening is given by $\sim(\lambda_1/\lambda_2)^{-1.7}$. If we adopt the same extinction here the $v = 1-0$ S(0) line could be underestimated by $\sim 7\%$ and the $v = 2-1$ S(1) line by 9% compared to the $v = 1-0$ S(1) line. We have not taken this into account in our analysis, as there are almost certainly small variations in extinction over OMC1 at the scale of our object. Furthermore these variations are of the order of the uncertainty we find in the models.

(iii) In order accurately to compare the emission from the three lines, it is necessary to perform an accurate registration of the three line maps. This has been done by using the positions of 11 stars found in all three maps. Image registration has been performed to better than ± 1 pixel (i.e. 27 mas or 1/5 of the PSF *FWHM*).

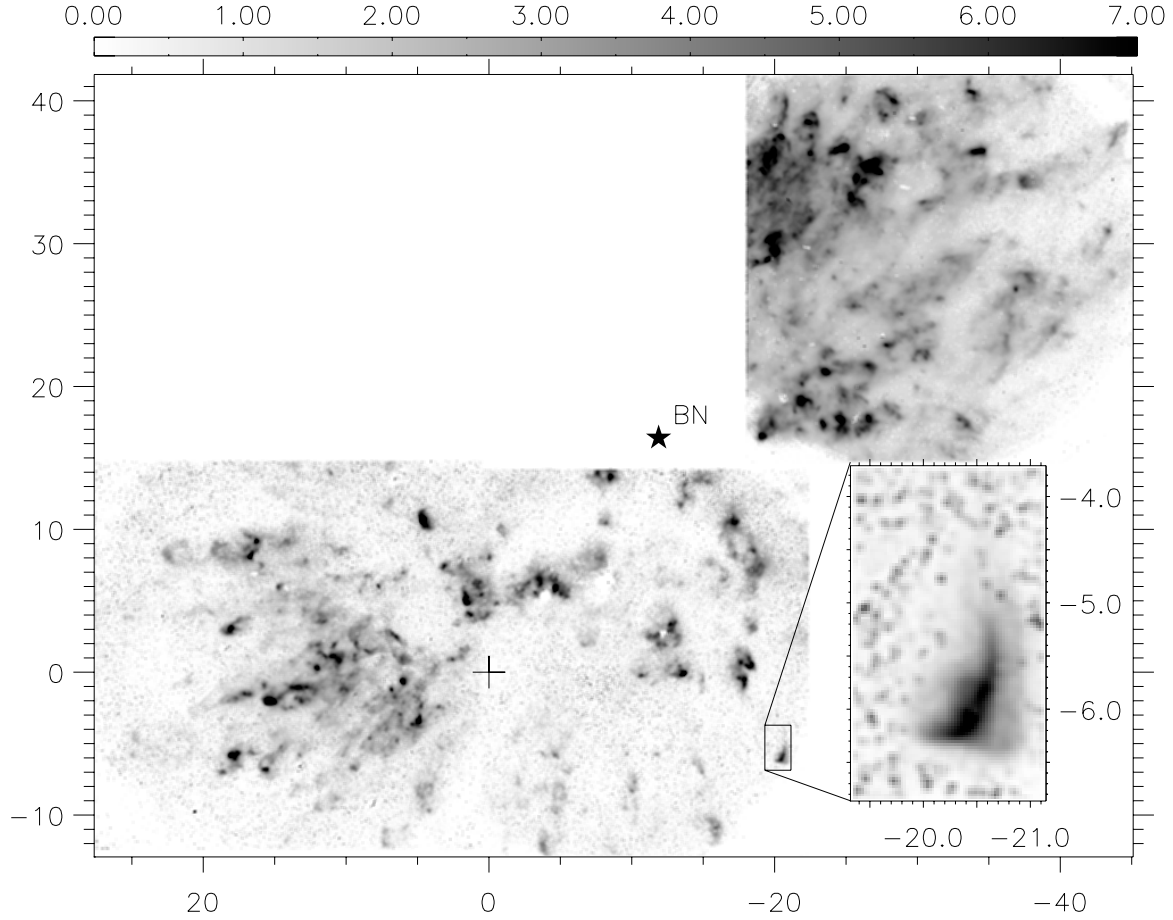


Fig. 1. Finding chart showing our 3 fields of view in the continuum-subtracted H₂ $v = 1-0$ S(0) line at 2.23 μm . The colour bar is in units of $10^{-6} \text{ W m}^{-2} \text{ sr}^{-1}$, and the coordinates are given in arcseconds with respect to TCC0016 ($05^{\text{h}}35^{\text{m}}14^{\text{s}}.91$, $-05^{\circ}22'39''.31$; J2000). The position of the star TCC0016 is marked with a cross (+) and the BN object is marked with a star (*). The inset shows a zoom of the shock delineated by the rectangle.

3. Results and 2D model description

We choose to limit this paper to the description of one bow shock in our field of view. In a forthcoming paper we will report a more systematic analysis of a larger selection of bow shocks found in our field of view. The present object is located $20''.5$ W and $6''$ S of TCC0016, our positional reference point ($05^{\text{h}}35^{\text{m}}14^{\text{s}}.91$, $-05^{\circ}22'39''.31$; J2000). The object is shown in the inset in Fig. 1 in $v = 1-0$ S(0) emission. The peak brightness in the strong $v = 1-0$ S(1) line is $(2.06 \pm 0.09) \times 10^{-5} \text{ W m}^{-2} \text{ sr}^{-1}$, whereas it is 3.3 times lower in the $v = 1-0$ S(0) line and 5.6 times lower in the $v = 2-1$ S(1) line.

This object has previously been described in Kristensen et al. (2007) (labelled object 3) and Nissen et al. (2007) (labelled B43). In Kristensen et al., it was found that a shock with velocity $\sim 35-40 \text{ km s}^{-1}$ and preshock density $\sim 10^5 \text{ cm}^{-3}$ could reproduce the line brightness of the $v = 1-0$ S(1) and $v = 1-0$ S(0) H₂ lines. Those data showed a spatial resolution of $0''.45$ and were obtained with the 3.6 m Canada-France-Hawaii telescope (CFHT). In that analysis the shock width was also used as an observational constraint. The shock width was obtained from ESO-VLT/NACO observations where the spatial resolution was 80 mas (Lacombe et al. 2004).

Using the GriF FP interferometer on CFHT Nissen et al. (2007) measured radial velocities of H₂ emitting in the $v = 1-0$ S(1) line. They measured a peak radial velocity of -36 km s^{-1} , that is, the object is moving towards us at

$36 \pm 1 \text{ km s}^{-1}$. Recent proper motion studies performed by Cunningham (2006) indicate that this object has a proper motion of $41 \text{ km s}^{-1} \pm 25 \text{ km s}^{-1}$. The full 3D velocity of this object is then $\sim 55 \pm 25 \text{ km s}^{-1}$ and the angle with respect to the plane of the sky is $\sim 40^{\circ} \pm 27^{\circ}$.

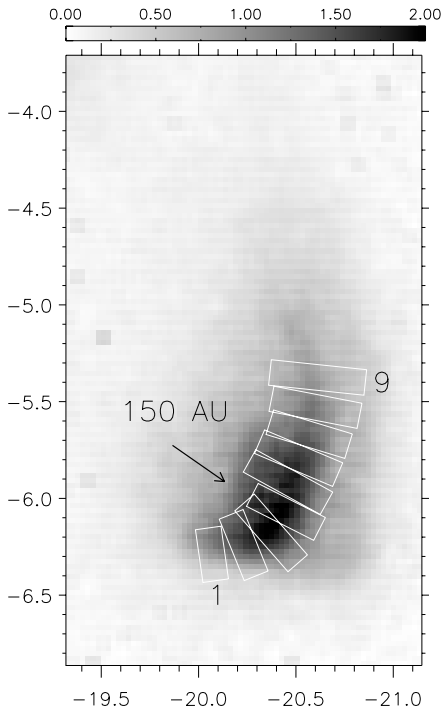
In the bow shock we seek to reproduce line emission properties along the bow thus predicting physical conditions along the bow. We do this by slicing the bow into 9 segments shown in Fig. 2, with a width corresponding to the resolution ($0''.15 \sim 70 \text{ AU}$). We align each of the segments so they are perpendicular to the bow front. In order to define the bow shape we have chosen to fit two parabolic curves to the points of maximum brightness along the bow, one for each side of the bow. We fit each side of the brightest pixel in the bow with a different parabolic curve as the object is slightly asymmetric.

Reverting to a simpler model using a single parabola we determine the position angle to be 235° . This angle has been determined by rotating the shock in steps of 5° and fitting a single parabola to the location of the peaks in brightness and calculating χ^2 . At an angle of 235° we find a minimum in χ^2 and we choose this as our position angle. In Sects. 4.3.1 and 4.3.2 we refine this choice.

This is higher than the position angle given by Cunningham (2006) of 184° and of Nissen et al. (2007) (221°). The position angle given in Nissen et al. is very close to the position angle towards radio source I and source n (223°) both likely

Table 1. Characteristics of the 9 segments of the bow object described in the text and displayed in Fig. 2. Brightness is given in units of $10^{-5} \text{ W m}^{-2} \text{ sr}^{-1}$ and $FWHM$ perpendicular to the bow surface in units of AU. The uncertainties σ_{obs} given are 1σ .

Segment	Position angle	Brightness ($10^{-5} \text{ W m}^{-2} \text{ sr}^{-1}$)				$FWHM$ (AU)	
		$v = 1-0 \text{ S}(1)$	$v = 1-0 \text{ S}(0)$	$v = 2-1 \text{ S}(1)$	$v = 1-0 \text{ S}(1)$	$v = 1-0 \text{ S}(0)$	$v = 2-1 \text{ S}(1)$
1	188°	0.86 ± 0.03	0.32 ± 0.02	0.18 ± 0.01	130 ± 30	100 ± 60	80 ± 70
2	202°	1.24 ± 0.04	0.44 ± 0.02	0.28 ± 0.02	160 ± 20	130 ± 40	120 ± 50
3	221°	1.55 ± 0.05	0.50 ± 0.02	0.32 ± 0.02	190 ± 15	170 ± 20	140 ± 40
4	243°	1.57 ± 0.05	0.53 ± 0.02	0.29 ± 0.02	180 ± 15	160 ± 20	140 ± 40
5	241°	1.42 ± 0.05	0.45 ± 0.02	0.26 ± 0.01	210 ± 15	160 ± 20	180 ± 30
6	247°	1.32 ± 0.04	0.47 ± 0.02	0.24 ± 0.01	200 ± 15	130 ± 20	160 ± 30
7	253°	1.05 ± 0.04	0.41 ± 0.02	0.21 ± 0.02	200 ± 20	120 ± 40	160 ± 40
8	259°	0.87 ± 0.03	0.34 ± 0.02	0.16 ± 0.01	210 ± 25	140 ± 50	170 ± 50
9	264°	0.70 ± 0.03	0.28 ± 0.02	0.11 ± 0.01	230 ± 30	110 ± 60	150 ± 60

**Fig. 2.** Location and extent of the 9 segments we have chosen to study overlaid on a map of continuum subtracted H₂ $v = 1-0 \text{ S}(1)$ emission. Coordinates are relative to TCC0016 and the colorbar is given in units of $10^{-5} \text{ W m}^{-2} \text{ sr}^{-1}$. The location of the shock is shown in Fig. 1. We have labelled segments 1 and 9 for easy identification. The arrow shows a position angle of 235° and the length corresponds to 150 AU.

candidates as the source of the outflow (Nissen et al. 2007, and references therein). Given the uncertainty of our method ($\pm 10^\circ$) and the uncertainty in the angle determined by Nissen et al. ($\pm 5^\circ$) there is no significant disagreement. Based on the data given in Cunningham we estimate that the 1σ uncertainty is of the order of $\sim 55^\circ$. Thus our result for the position angle agrees with that of Cunningham (2006). The position angles of the individual segments are listed in Table 1.

We now average the segments in the direction perpendicular to the bow to increase the S/N ratio. For each segment along the bow we obtain a brightness profile perpendicular to the bow (see Fig. 3). This is done for all of the three H₂ rovibrational lines. We measure the $FWHM$ of the 3 brightness profiles observed illustrated by the box lengths in Fig. 2. We then average the brightness over the $FWHM$ of the profile. $FWHM$ is chosen because it does not depend on the noise level. For the segments

analysed here, the $FWHM$ is always measured well above the noise level, which is also clear from Fig. 3.

For each segment we thus have 6 observational constraints:

- $FWHM$ measurements of emission perpendicular to the bow profile for each of the 3 lines.
- line brightness of the H₂ lines $v = 1-0 \text{ S}(1)$, $v = 1-0 \text{ S}(0)$ and $v = 2-1 \text{ S}(1)$ averaged over the $FWHM$ of the bow profile.

In Fig. 2 we display the location and extent of each segment and in Table 1 we list the 6 observational constraints for the segments and we display them in Figs. 4 and 5. For the moment we have chosen not to include the velocity as an observational constraint for the following reason. We do not know how the proper motion changes along the bow. Thus we only know the peak or apex velocity. In order to use the velocity as a constraint it would have been necessary to have detailed information of the measured 3D velocities along the bow and to take the inclination of the shock into account. The model we construct here is a 2D model ignoring any effects of inclination with respect to the plane of the sky.

As can be seen from VLT images in these observations and those of Lacombe et al. (2004), the object is elongated along the direction of motion (Cunningham 2006) near the centre. This can be seen as a secondary brightness peak slightly upstream around 50 AU in segments 3–6 in Fig. 3. The separation between the two centres of brightness is $\sim 55 \text{ AU}$ ($0''.12$) which is comparable to our resolution. The position angle between the two is $\sim 206^\circ \pm 20^\circ$. This is consistent with the position angle determined here as well as the position angle determined in the proper motion studies by Cunningham (2006) and radial velocity measurements by Nissen et al. (2007). This secondary brightness may be due to a Mach disk. For the moment we choose to ignore this, but we will return to it in Sect. 4.4.3.

4. Shock model

4.1. Model description

We use the plane parallel (1D) steady state, multi-fluid shock model described in Flower & Pineau des Forêts (2003) and references therein. Here we will describe the parts of the model important for our analysis.

In the models the magnetohydrodynamic equations are integrated in parallel with chemical reaction rate equations in a self-consistent manner. For each step of the model, abundances of 136 species linked by 1040 reactions are calculated. The initial species abundances are given by Flower & Pineau des Forêts (2003). In particular we mention here that the initial PAH-abundance is set to $n_{\text{PAH}}/n_{\text{H}} = 10^{-6}$. This has important

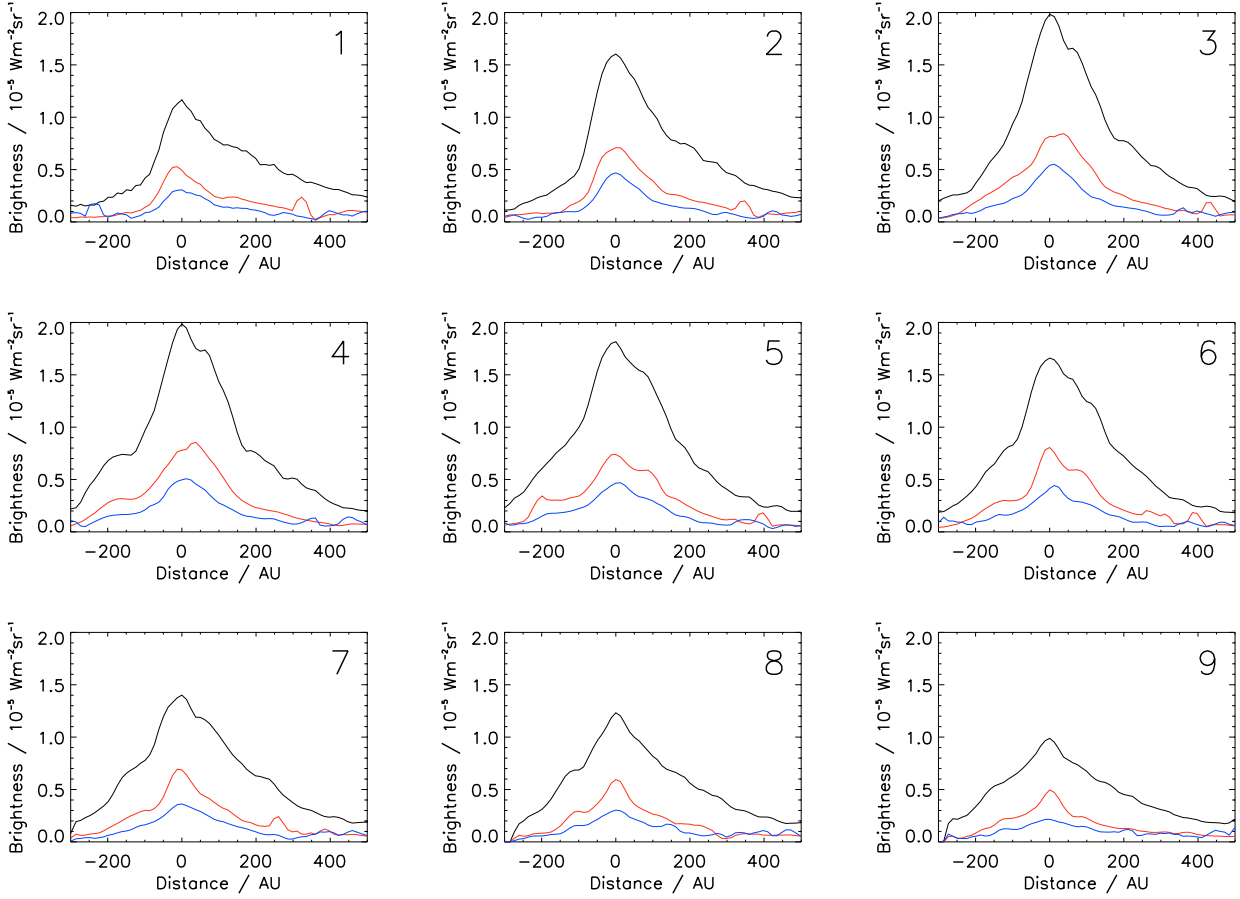


Fig. 3. Intensity cuts through the bow of the H₂ $v = 1-0$ S(1) (black), $v = 1-0$ S(0) (red) and $v = 2-1$ S(1) (blue) lines in each segment. Distances are given in AU and the zero point is the location of the brightness maximum. This point does not change significantly for the other two lines. Negative distances indicate that this brightness is outside the bow, while positive distances are inside. The number in each profile refers to the segment number (see Fig. 2).

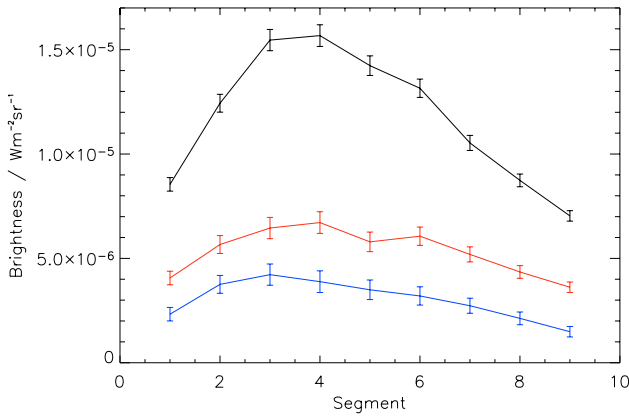


Fig. 4. Brightness averaged over the *FWHM* along the bow for the three lines $v = 1-0$ S(1) (black), $v = 1-0$ S(0) (red) and $v = 2-1$ S(1) (blue) in each segment. Error bars show 1σ uncertainties.

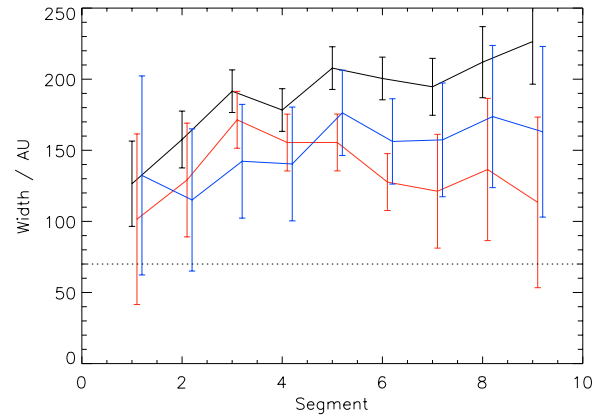


Fig. 5. *FWHM* of H₂ emission for the three lines $v = 1-0$ S(1) (black), $v = 1-0$ S(0) (red) and $v = 2-1$ S(1) (blue) in each segment. The dotted line at 70 AU shows the spatial resolution (see text). Errorbars show 1σ uncertainties. Points representing $v = 1-0$ S(0) and $v = 2-1$ S(1) widths have been shifted horizontally by 0.1 and 0.2 respectively so as to clearly separate the error bars.

consequences for the magnetosonic speed of the charged fluid and therefore the maximum velocity we can achieve in C-type shocks (Flower & Pineau des Forêts 2003). Furthermore 100 H₂ rovibrational level populations are calculated at each step. This includes transitions between rovibrational levels.

In the models the transverse component of the magnetic field is assumed frozen into the charged fluid of the preshock gas. The transverse preshock magnetic field strength is given by

$b \times n_{\text{H}}^{1/2} \mu\text{Gauss}$ where b is the magnetic scaling factor and n_{H} is the number of hydrogen nuclei in units of cm^{-3} in the preshock gas. b is typically between 0 and 10. The cosmic ray ionization rate is set to $5 \times 10^{-17} \text{ s}^{-1}$ per H atom.

Table 2. Input parameters of the models which best reproduce observations. Results (confidence intervals) are listed for each segment (see Fig. 2).

Segment	Preshock density (cm ⁻³)	Shock velocity (km s ⁻¹)	<i>b</i>	<i>o/p</i> _{ini}
1	5 × 10 ⁵ (5 × 10 ⁵ –10 ⁶)	38 (29–39)	3.5 (2.0–4.5)	3.00 (0.01–3.0)
2	5 × 10 ⁵ (5 × 10 ⁵ –10 ⁶)	42 (37–45)	4.0 (3.0–6.5)	3.00 (2.0–3.0)
3	5 × 10 ⁵ (5 × 10 ⁵ –10 ⁶)	49 (41–50)	6.0 (4.5–8.5)	3.00 (2.0–3.0)
4	5 × 10 ⁵ (5 × 10 ⁵ –10 ⁶)	47 (40–50)	5.0 (4.0–8.0)	3.00 (2.0–3.0)
5	5 × 10 ⁵ (5 × 10 ⁵ –10 ⁶)	46 (39–49)	5.0 (4.0–8.0)	3.00 (2.0–3.0)
6	5 × 10 ⁵ (5 × 10 ⁵ –10 ⁶)	44 (39–45)	4.5 (3.5–6.5)	3.00 (2.0–3.0)
7	5 × 10 ⁵ (5 × 10 ⁵ –10 ⁶)	41 (36–43)	4.0 (2.5–5.0)	3.00 (2.0–3.0)
8	5 × 10 ⁵ (5 × 10 ⁵ –10 ⁶)	38 (37–42)	3.5 (3.0–6.5)	3.00 (2.0–3.0)
9	5 × 10 ⁵ (5 × 10 ⁵)	35 (32–39)	3.0 (2.0–4.5)	3.00 (0.01–3.0)

Recently a grid of ~25 000 models was calculated (Kristensen et al. 2007, in preparation) and we use these results. The grid covered the following four input parameter ranges (with corresponding step sizes):

- preshock density: 10⁴, 5 × 10⁴, 10⁵, 5 × 10⁵, 10⁶, 5 × 10⁶, 10⁷ cm⁻³;
- shock velocity: 10–50 km s⁻¹ (step size: 1 km s⁻¹);
- magnetic scaling factor, *b*: 0.0–10.0 (step size: 0.5);
- initial H₂ ortho/para ratio: 0.01, 1.0, 2.0, 3.0.

The grid includes both C(ontinuous)-type shocks and J(ump)-type shocks. For J-type shocks we set the magnetic scaling factor to 0.0 and 0.1.

4.2. C- versus J-type shock

In the following we will only consider C-type shocks and C-type shocks with a small J-type component for the following two reasons.

- (i) [FeII] emission at the heart of OMC1 is primarily observed around well-known HH-objects such as HH208 (Schultz et al. 1999) and the Orion bullets (e.g. Allen & Burton 1993). For the object we examine here, no [FeII] emission has been observed (Takami et al. 2002). Therefore it is likely that the shock observed is not dissociative (Kristensen et al. 2007, in preparation). Given the relatively high velocity (~40–60 km s⁻¹; Cunningham 2006; Nissen et al. 2007) J-type shocks are fully dissociative and we would expect a brightness of the strong [FeII] line at 1.257 μm of ~10⁻⁷ W m⁻² sr⁻¹ (Kristensen et al. 2007, in preparation) which is above the noise limit of Takami et al. (2002). In a C-type shock very little [FeII] emission is predicted (i.e. less than 10⁻⁸ W m⁻² sr⁻¹) along with very little or no H₂ dissociation.
- (ii) The *FWHM* of the H₂ emission in the different segments is observed to be ≥100 AU. In J-type shocks this is impossible to reproduce, even with a weak component of the transverse magnetic field (Kristensen et al. 2007, in preparation). The width is however readily reproduced by C-type shock models, where widths between 1 and 10⁵ AU can be achieved, depending on initial conditions.

We do not exclude the presence of J-type shocks in OMC1. As has previously been shown (e.g. Brand et al. 1988, 1989; Moorhouse et al. 1990) H₂ excitation of the *v* = 3 and 4 levels cannot be reproduced by C-type shock models. Therefore part of the excitation mechanism may be due to PDR excitation and/or J-type shocks (Kristensen et al. 2003). For the object under study, emission arising from J-type shocks is probably weak. At this stage we do not rule out that there may be an

additional J-type component in the observed (C-type) shock. If such a component exists, it would be located close to the apex (see Sect. 4.4.4).

4.3. Reproduction of observations

We will now attempt to reproduce the observed properties (line brightness and width) for all segments of the object. We do this by fitting a plane parallel C-type shock model to each segment. We are interested in obtaining values for the preshock density, shock velocity, transverse magnetic field strength and the value of the initial H₂ ortho/para (*o/p*) ratio.

To reproduce the observed brightness we have extracted the brightness and width from the models in the same manner as in the observations. That is, for every 1D shock model we have calculated the emissivity profile of each of our H₂ lines as a function of distance along the shock. We have measured the spatial extent of the *FWHM* of our emissivity profile and we use this to compare with our observed *FWHM*. The emissivity profile is then integrated over the *FWHM* to yield the brightness. In this last step, we are implicitly assuming that the average depth in the line of sight of the shock in each segment is comparable to the *FWHM* given in Table 1, Cols. 6–8.

Values corresponding to the six observational constraints (three line brightness and three widths) were extracted from the models and we use a χ² analysis to determine how well individual models reproduce the observations. For each model we thus calculate χ² = $\frac{1}{n} \sum \left(\frac{X_{\text{obs}} - X_{\text{model}}}{\sigma_{\text{obs}}} \right)^2$ where *n* is the number of observational constraints (i.e. six), *X*_{obs} and *X*_{model} refer to observed and modelled property respectively and σ_{obs} is the observed uncertainty. These are all given in Table 1.

For each segment we list the best fit models with corresponding confidence intervals in Table 2 and show our results in Fig. 7. The results are as follows:

- the shock speed decreases from ~50 km s⁻¹ at the apex to ~40 km s⁻¹ in the southern wing (segment 1, Fig. 2) and ~35 km s⁻¹ in the northern wing (segment 9, Fig. 2);
- the magnetic scaling factor *b* varies from ~6.0 at the apex to ~3.5 in the southern wing and to ~3.0 in the northern wing;
- the density is constant at 5 × 10⁵ cm⁻³.
- the initial *o/p* ratio does not change from 3. This is the value the *o/p* ratio is expected to have at high temperatures (i.e. greater than 300 K).

In Fig. 6 we show the local brightness profile of the *v* = 1–0 S(1) line as well as the kinetic temperature profile. This is shown for the model corresponding to the best fit model of segment 3, which is the segment containing the apex of the shock. The figure shows that the *v* = 1–0 S(1) *FWHM* is 97 AU, that

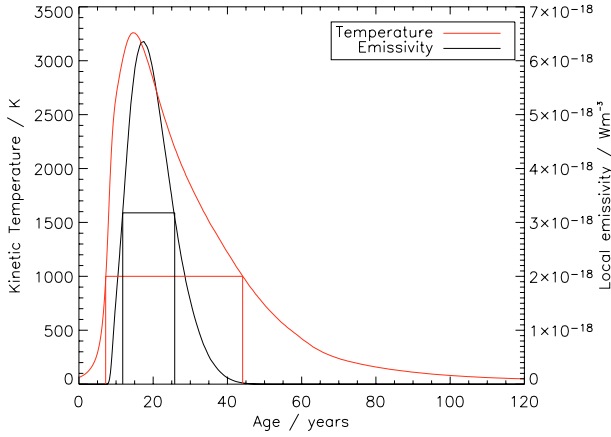


Fig. 6. Emissivity profile of the $v = 1-0$ S(1) H₂ line of the shock model corresponding to the best fit of segment 3 (the apex of the shock). Preshock density is $5 \times 10^5 \text{ cm}^{-3}$, shock velocity 49 km s^{-1} , b is 6.0 and the initial o/p ratio is 3.0. We also display the kinetic temperature (red). The $FWHM$ of the H₂ profile is 14 years (97 AU; marked by vertical black lines) and the width of the shock at a temperature of 1000 K is 37 years (216 AU; marked by red vertical lines). At a temperature of 50 K the width is 120 years (489 AU; the size of the abscissa).

is the width is underestimated by 51% (the observed $FWHM$ is 190 AU, see Table 1). The total size of the H₂ emitting zone corresponds very well to the zone in which the kinetic temperature is greater than 1000 K. The size of this zone is 216 AU. The time to reach steady-state at 50 K is 120 years.

We now discuss what can be learned from these results.

4.3.1. Shock velocity

It is possible to compare our predicted peak velocity to the measured 3D velocity. The measured 3D velocity is $\sim 55 \text{ km s}^{-1} \pm 25 \text{ km s}^{-1}$ (Nissen et al. 2007; Cunningham 2006) and we predict a shock velocity of $\sim 50 \text{ km s}^{-1}$. Thus there is good agreement between our results. Furthermore we predict how the velocity will change along the bow as illustrated in Fig. 7.

If the bow shape remains steady over time, the shock velocity perpendicular to the bow surface should vary along the bow as

$$v_{\perp} = v_0 \times \cos(pa - pa_0) \quad (1)$$

where v_0 is the maximum velocity, pa the position angle of the given segment and pa_0 the position angle of the bow motion. In Fig. 8 we show the velocity component perpendicular to the surface and the best fit results of Eq. (1). As a result we find that the position angle for the bow shock is $224^{\circ} \pm 3^{\circ}$ and that the maximum velocity is $47 \text{ km s}^{-1} \pm 2 \text{ km s}^{-1}$. The position angle is in agreement with other position angles as discussed in Sect. 3.

With future high spatial resolution observations of this object it should be possible to observe the proper motion of the individual segments. If the shock is moving at an angle of $\sim 40^{\circ}$ with respect to the plane of the sky, then at a spatial resolution of ~ 0.15 it should be possible to resolve the differential motion over a period of 13 years.

4.3.2. Transverse magnetic field

If we assume that the magnetic field is uniform, we may deduce its position angle, pa_B . This position angle is determined in much the same way as the position angle of the shock above.

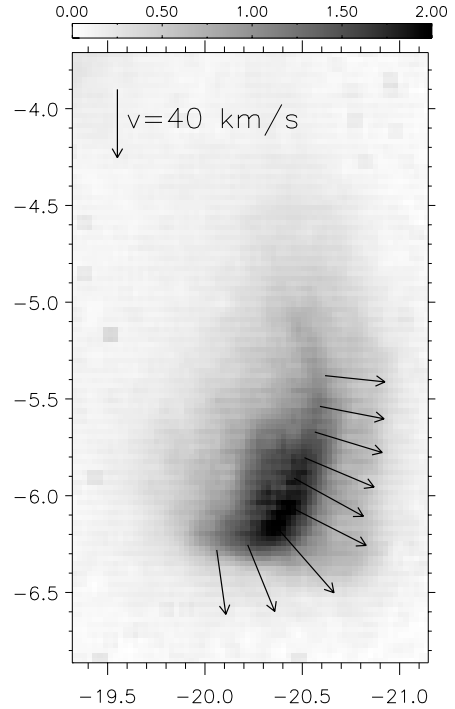


Fig. 7. Velocity variations along the bow superposed on an image of the bow shock as observed in $v = 1-0$ S(1). Coordinates and colour bar are as in Fig. 2. The lengths of the arrows are scaled with velocity and the arrow in the top left corner has a length corresponding to 40 km s^{-1} .

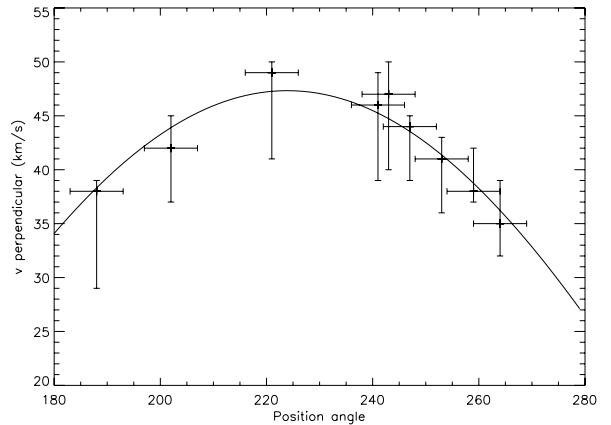


Fig. 8. Shock velocity perpendicular to the bow, as a function of position angle. The curve shows the best-fit solution to Eq. (1).

Quantitatively we compare the changes in the magnetic field tangential to the bow with a simple model where

$$b_{\parallel} = b_0 \times \cos[(pa \pm \pi/2) - pa_B] = b_0 \times |\sin(pa - pa_B)| \quad (2)$$

as in Eq. (1). Here b_0 is the maximum value of the magnetic scaling factor and $(pa \pm \pi/2)$ is the position angle of the local tangent to the bow surface. This is shown in Fig. 9.

With this model we find that $b_0 = 4.8 \pm 0.7$ and pa_B is $132^{\circ} \pm 16^{\circ}$. Observations of polarized light in the region (e.g. Hough et al. 1986; Chrysostomou et al. 1994; Simpson et al. 2006; Tamura et al. 2006) indicate that the magnetic field has a position angle of $\sim 140^{\circ}$. The position angle of our shock was determined to $224^{\circ} \pm 3^{\circ}$ above. Therefore we conclude that the magnetic field is oriented tangentially to the apex.

The predicted magnetic field strength is $\sim 3.4 \pm 0.5 \text{ mGauss}$ at the apex. This value may be compared with magnetic fields

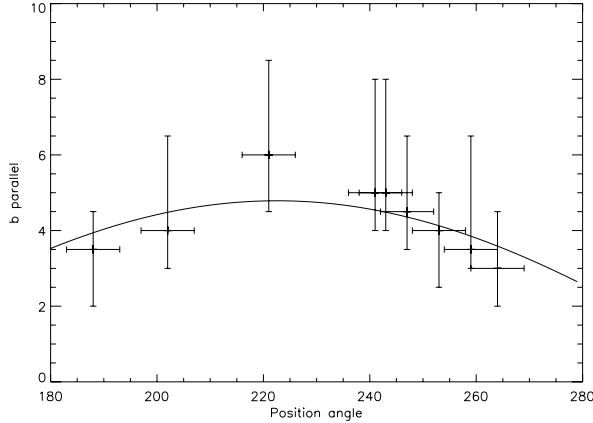


Fig. 9. Magnetic scaling factor b , as a function of position angle. The curve shows the best-fit solution to Eq. (2).

derived from observations made by Norris (1984), Chrysostomou et al. (1994) and Crutcher et al. (1999). They find that the magnetic field near IRC2 is ~ 3 mGauss (Norris 1984) and that it is of the order of 0.3 mGauss $24''$ north of IRC2 (Crutcher et al. 1999). Chrysostomou et al. (1994) estimate the Alfvén velocity by measuring the dispersion of polarized $v = 1-0$ S(1) emission. From this they find that $b = 10$.

4.3.3. Density

We do not predict that the preshock density changes along the bow. This indicates that the medium here is not clumpy on scales of the size of this bow shock (~ 600 AU), or that the density variations in the medium are sufficiently small that they cannot be detected here.

4.3.4. Initial ortho/para ratio

The initial o/p ratio is in all segments equal to 3. In Kristensen et al. (2007) the initial o/p ratio could not be determined although observations suggested it is lower than the high temperature equilibrium value of 3. If we lock the initial o/p ratio in our χ^2 analysis, we find that the value of χ^2 change by less than 5% no matter what the initial o/p ratio is. This implies that for our observations we cannot determine the initial o/p ratio.

4.4. Discussion of sources of error

For the above modelling there are four main sources of error. These sources are as follows:

- Geometrical effects: we ignore the inclination of the shock and the depth of emission.
- We do not consider photo-excitation by the massive O6 star, θ^1 Ori C, located in the Trapezium at a projected distance of ~ 0.13 pc ($\sim 27\,000$ AU).
- There may be a possible Mach disk located behind the apex of the bow. This is not included in our analysis.
- At the apex there may be an additional J-type shock component which is not spatially resolved in our observations.

4.4.1. Geometrical effects

The main assumption in constructing the 2D model is that the object is observed sufficiently edge-on that we can ignore the true inclination of the object with respect to the plane of the sky.

As seen in Sect. 3 the actual inclination of the object is $\sim 40^\circ$ with respect to the plane of the sky. Assuming that the width scales with $\sin i$, where i is the inclination angle, the width may be overestimated by $\sim 25\%$. This is about twice the observational uncertainty for the width in the strong $v = 1-0$ S(1) line and smaller in the two other weaker lines.

If the width is smaller, then we would have overestimated our preshock density and underestimated the transverse magnetic field strength and shock velocity (Kristensen et al. 2007, in preparation). Based on observations, it is unlikely that the transverse magnetic field is higher (Norris 1984). The proper velocity of the object is ~ 55 km s $^{-1}$, whereas we predict 47 km s $^{-1}$. For a shock with velocity 55 km s $^{-1}$, preshock density 5×10^5 cm $^{-3}$ and magnetic scaling factor $b = 6.0$, the *FWHM* of the local emission of the $v = 1-0$ S(1) line is ~ 100 AU below the observed width of ~ 150 AU.

If the density is lowered to 10^5 cm $^{-3}$, the *FWHM* of the $v = 1-0$ S(1) line is ~ 400 AU, or more than twice the observed *FWHM* of the line. It is probably possible to fine tune the input parameters, but that would require a grid of shock models with a higher resolution than we used.

4.4.2. The PDR created by θ^1 Ori C

As shown by Kristensen et al. (2003) the PDR generated by θ^1 Ori C in the neighbouring Peak 2 (southeast of BN) is of the order of 10–15% in bright objects. We reexamine this here for the shock analyzed in the present work. We compare our results with those of the “Meudon PDR code” (Le Petit et al. 2006).

For a density of 5×10^5 cm $^{-3}$ and a radiation field of the order of 10^5 times the standard interstellar field (Draine 1978), the PDR models predict a brightness in $v = 1-0$ S(1) more than an order of magnitude lower than observed. Even if the density is increased to 10^6 cm $^{-3}$ it is impossible to reproduce the $v = 1-0$ S(1) brightness.

The $v = 1-0$ S(1) / $v = 2-1$ S(1) line ratio is often used as a shock/PDR discriminant. Here we observe a relatively low value of this ratio, the average over all segments is 5.2. This ratio is easily reproduced by PDR-models for the above conditions (Le Petit et al. 2006). However, as for the $v = 1-0$ S(1) line above, the absolute brightness is underestimated by an order of magnitude. Therefore we conclude that the contribution from the PDR generated by θ^1 Ori C is less than or equal to 10% of the total emission, and we ignore it.

This is in agreement with the contribution estimated in Kristensen et al. (2003). It should be noted here that the uncertainty of the $v = 1-0$ S(1) brightness is of the order of $\sim 3-10\%$ reddening apart. Lowering the brightness by $\sim 10\%$ would imply that we are overestimating the preshock density and shock velocity while underestimating the transverse magnetic field.

4.4.3. Existence of Mach disk

Behind the apex of the bow shock there is a small clump of brightly emitting gas. The distance between this clump and the apex is ~ 0.3 . It is at this location that Nissen et al. (2007) reports a peak in radial velocity. The brightness is $\sim 1.5 \times 10^{-5}$ W m $^{-2}$ sr $^{-1}$ on average. From the position and velocity structure this emission may well arise from a Mach disk. In this connection, a Mach disk is not included in the shock models and we may thus have made an overestimate of the width of the shock, particular in the central parts (i.e. segments 3–6, see Fig. 3). We have already discussed the consequences of overestimating the width above, see Sect. 4.4.1.

4.4.4. J-type shock component of the bow shock

We have assumed that we are observing a shock in steady-state. If there is a non steady-state component of the shock, this will show up as a J-type shock component (Chièze et al. 1998; Lesaffre et al. 2004). Non steady-state shocks are typically seen if the dynamical age of the shock is shorter than the steady-state age.

The projected distance between this object and the possible outflow source, radio source I (e.g. Menten & Reid 1995; Greenhill et al. 2004; Nissen et al. 2007), is ~ 47 mpc (10^4 AU). At a velocity of ~ 50 km s⁻¹ the dynamical age is ≥ 1000 yrs consistent with the dynamical age of the Orion bullets (Doi et al. 2002). This may be compared to the steady-state timescale for a shock with preshock density 5×10^5 cm⁻³, shock velocity 50 km s⁻¹ and magnetic scaling factor $b = 6.0$ which is ~ 120 yrs. Here we measure steady-state shock widths and ages at a kinetic temperature of the post shock gas of 50 K (Wilgenbus et al. 2000).

Because the dynamical age is an order of magnitude greater than the steady-state timescale, we conclude that it is unlikely there is a non steady-state component of the shock. If the width of the shock is decreased (as discussed above), the time required to reach steady state is shorter, strengthening the argument that the shock is a steady-state shock.

5. Concluding remarks

We have introduced a more sophisticated means of reproducing observations of bow shocks observed at high spatial resolution. This new method allows us in the example considered to predict a peak velocity of the bow shock which is in very good agreement with results from radial velocity and proper motion observations. Furthermore our predictions of the direction and strength of the magnetic field are consistent with independent estimates. These include observations which analyse the line-of-sight component of the magnetic field and the total magnetic field as well as polarization observations of the region. Our prediction of how the magnetic field strength changes along the bow is in agreement with a simple geometrical model, where the apex is moving perpendicular to the magnetic field.

The data we have for most of the central part of OMC1 show that it would be possible to apply this new method on numerous objects which appear to be caused by shocks. The main requirement is that the shocks are moving close to the plane of the sky. Preliminary results from 3D modelling shows that this requirement is fulfilled when the angle with respect to the plane of the sky is less than 50° (Ravkilde et al. 2007). Shocks moving along the line-of-sight are naturally not suitable candidates.

Not only do the results presented here provide a new insight into the physics of bow shocks, it will also serve as a starting point for a full 3D bow shock model currently under construction (Ravkilde et al. 2007).

Acknowledgements. We would like to thank the referee, M. Burton, for his very constructive comments, which have improved this paper. L.E.K., S.D. and J.L.L. would like to acknowledge the support of the PCMI National Programme, funded by the CNRS in cooperation with the CEA and IN2P3. T.L.R. and D.F. would like to acknowledge the support of the Aarhus Centre for Atomic Physics (ACAP), funded by the Danish Basic Research Foundation. We also wish to thank the Directors and Staff at ESO for making possible the observations reported in this paper. Part of this work was performed using computer resources at the Université de Cergy-Pontoise.

References

- Allen, D. A., & Burton, M. G. 1993, *Nature*, 363, 54
 Axon, D. J., & Taylor, K. 1984, *MNRAS*, 207, 241
 Bally, J., & Zinnecker, H. 2005, *AJ*, 129, 2281
 Bally, J., O'Dell, C. R., & McCaughrean, M. J. 2000, *AJ*, 119, 2919
 Beckwith, S., Persson, S. E., Neugebauer, G., & Becklin, E. E. 1978, *ApJ*, 223, 464
 Beuther, H., Zhang, Q., Greenhill, L. J., et al. 2004, *ApJ*, 616, L31
 Brand, P. W. J. L., Moorhouse, A., Burton, M. G., et al. 1988, *ApJ*, 334, L103
 Brand, P. W. J. L., Toner, M. P., Geballe, T. R., et al. 1989, *MNRAS*, 236, 929
 Chièze, J.-P., Pineau des Forêts, G., & Flower, D. R. 1998, *MNRAS*, 295, 672
 Chrysostomou, A., Hough, J. H., Burton, M. G., & Tamura, M. 1994, *MNRAS*, 268, 325
 Chrysostomou, A., Burton, M. G., Axon, D. J., et al. 1997, *MNRAS*, 289, 605
 Crutcher, R. M., Troland, T. H., Lazareff, B., Paubert, G., & Kazès, I. 1999, *ApJ*, 514, L121
 Cunningham, N. J. 2006, Ph.D. Thesis, University of Colorado
 Doi, T., O'Dell, C. R., & Hartigan, P. 2002, *AJ*, 124, 445
 Draine, B. T. 1978, *ApJS*, 36, 595
 Elmegreen, B. G., & Lada, C. J. 1977, *ApJ*, 214, 725
 Flower, D. R., & Pineau des Forêts, G. 2003, *MNRAS*, 343, 390
 Fragile, P. C., Anninos, P., Gustafson, K., & Murray, S. D. 2005, *ApJ*, 619, 327
 Gezari, D. Y., Backman, D. E., & Werner, M. W. 1998, *AJ*, 116, 1816
 Giannini, T., McCoey, C., Nisini, B., et al. 2006, *A&A*, 459, 821
 Gómez, L., Rodríguez, L. F., Loinard, L., et al. 2005, *ApJ*, 635, 1166
 Greenhill, L. J., Reid, M. J., Chandler, C. J., Diamond, P. J., & Elitzur, M. 2004, in *IAU Symp.*, ed. M. Burton, R. Jayawardhana, & T. Bourke, 155
 Gustafsson, M. 2006, Ph.D. Thesis, University of Aarhus, Denmark
 Gustafsson, M., Kristensen, L. E., Clénet, Y., et al. 2003, *A&A*, 411, 437
 Gustafsson, M., Lemaire, J., Hartung, M., & Field, D. 2007, in preparation
 Hillenbrand, L. A., Strom, S. E., Calvet, N., et al. 1998, *AJ*, 116, 1816
 Hough, J. H., Axon, D. J., Burton, M. G., et al. 1986, *MNRAS*, 222, 629
 Kristensen, L. E., Gustafsson, M., Field, D., et al. 2003, *A&A*, 412, 727
 Kristensen, L. E., Ravkilde, T. L., Field, D., Lemaire, J. L., & Pineau Des Forêts, G. 2007, *A&A*, 469, 561
 Lacombe, F., Gendron, E., Rouan, D., et al. 2004, *A&A*, 417, L5
 Le Petit, F., Nehmé, C., Le Bourlot, J., & Roueff, E. 2006, *ApJS*, 164, 506
 Lee, J.-K., & Burton, M. G. 2000, *MNRAS*, 315, 11
 Lee, C.-F., Stone, J. M., Ostriker, E. C., & Mundy, L. G. 2001, *ApJ*, 557, 429
 Lesaffre, P., Chièze, J.-P., Cabrit, S., & Pineau des Forêts, G. 2004, *A&A*, 427, 147
 Lim, A. J., Raga, A. C., Rawlings, J. M. C., & Williams, D. A. 2002, *MNRAS*, 335, 817
 Livingston, W., & Wallace, L. 1991, *An Atlas of the Solar Spectrum in the Infrared from 1850 to 9000 cm⁻¹*, N. S. O. Technical Report No. 91-001, Tech. rep., National Optical Astronomy Observatories
 Mathis, J. S. 1990, *ARA&A*, 28, 37
 McCaughrean, M. J., & Stauffer, J. R. 1994, *AJ*, 108, 1382
 Menten, K. M., & Reid, M. J. 1995, *ApJ*, 445, L157
 Moorhouse, A., Brand, P. W. J. L., Geballe, T. R., & Burton, M. G. 1990, *MNRAS*, 242, 88
 Neufeld, D. A., Melnick, G. J., Sonnentrucker, P., et al. 2006, *ApJ*, 649, 816
 Nissen, H. D., Gustafsson, M., Lemaire, J. L., et al. 2007, *A&A*, 466, 949
 Norris, R. P. 1984, *MNRAS*, 207, 127
 Ostriker, E. C., Lee, C.-F., Stone, J. M., & Mundy, L. G. 2001, *ApJ*, 557, 443
 Raga, A., & Cabrit, S. 1993, *A&A*, 278, 267
 Raga, A. C., de Gouveia Dal Pino, E. M., Noriega-Crespo, A., Mininni, P. D., & Velázquez, P. F. 2002, *A&A*, 392, 267
 Ravkilde, T. L., Kristensen, L. E., Cabrit, S., et al. 2007, in preparation
 Rosenthal, D., Bertoldi, F., & Drapatz, S. 2000, *A&A*, 356, 705
 Schultz, A. S. B., Colgan, S. W. J., Erickson, E. F., et al. 1999, *ApJ*, 511, 282
 Simpson, J. P., Colgan, S. W. J., Erickson, E. F., Burton, M. G., & Schultz, A. S. B. 2006, *ApJ*, 642, 339
 Skrutskie, M. F., Cutri, R. M., Stiening, R., et al. 2006, *AJ*, 131, 1163
 Smith, M. D., & Brand, P. W. J. L. 1990, *MNRAS*, 242, 495
 Smith, M. D., Davis, C. J., & Liou, A. 1997, *A&A*, 327, 1206
 Smith, M. D., Khanzadyan, T., & Davis, C. J. 2003, *MNRAS*, 339, 524
 Stolovy, S. R., Burton, M. G., Erickson, E. F., et al. 1998, *ApJ*, 492, L151
 Takami, M., Usuda, T., Sugai, H., et al. 2002, *ApJ*, 566, 910
 Tamura, M., Kandori, R., Kusakabe, N., et al. 2006, *ApJ*, 649, L29
 Vannier, L., Lemaire, J. L., Field, D., et al. 2001, *A&A*, 366, 651
 Wilgenbus, D., Cabrit, S., Pineau des Forêts, G., & Flower, D. R. 2000, *A&A*, 356, 1010